

GRANT
IN-34-CR
148086
P. 18

COMPUTATION OF INCOMPRESSIBLE VISCOUS FLOWS THROUGH TURBOPUMP COMPONENTS

Cetin Kiris and Leon Chang

(NASA-CR-192296) COMPUTATION OF
INCOMPRESSIBLE VISCOUS FLOWS
THROUGH TURBOPUMP COMPONENTS (MCAT
Inst.) 18 p

N93-20753

Unclass

G3/34 0148086

February 1993

NCC2-500

MCAT Institute
3933 Blue Gum Drive
San Jose, CA 95127

COMPUTATION OF INCOMPRESSIBLE VISCOUS FLOWS THROUGH TURBOPUMP COMPONENTS

CETIN KIRIS, and LEON CHANG

Abstract

Flow through pump components, such as an inducer and an impeller, is efficiently simulated by solving the incompressible Navier-Stokes equations. The solution method is based on the pseudocompressibility approach and uses an implicit-upwind differencing scheme together with the Gauss-Seidel line relaxation method. The equations are solved in steadily rotating reference frames and the centrifugal force and the Coriolis force are added to the equation of motion. Current computations use one-equation Baldwin-Barth turbulence model which is derived from a simplified form of the standard $k-\epsilon$ model equations. The resulting computer code is applied to the flow analysis inside a generic rocket engine pump inducer, a fuel pump impeller, and SSME high pressure fuel turbopump impeller. Numerical results of inducer flow are compared with experimental measurements. In the fuel pump impeller, the effect of downstream boundary conditions is investigated. Flow analyses at 80%, 100%, and 120% of design conditions are presented.

Introduction

Since the space launch systems in the near future are likely to rely on liquid rocket engines, increasing the efficiency and reliability of the engine components is an important task. One of the major problems in the liquid rocket engine is to understand fluid dynamics of fuel and oxidizer flows. Understanding the flow in the turbopump through numerical simulation will be of significant value toward finding better design which is simpler yet more efficient and robust with less manufacturing costs. Until recently, the pump design process was not significantly different from that of decades ago. Current semi-empirical turbomachinery design process does not account for the three-dimensional (3-D) viscous phenomena in the pump flows. Some of these 3-D viscous phenomena include wakes, the boundary layers in the hub, shroud and the blades, junction flows, and tip clearance flows. In order to meet the challenge of improving propulsion devices, NASA Marshall Space Flight Center (MSFC) has established a consortium involving universities, industries and NASA¹⁻².

Even though computational fluid dynamics (CFD) applications in turbines have been reported widely in the literature³⁻⁵, the applications in the pump area are quite limited. The objective of this report is to present, evaluate, and validate a computational procedure that solves incompressible Navier-Stokes equations for the pump components. For CFD to have an impact in the design procedure of the pump, a robust, efficient, and accurate scheme is required. In addition, the algorithm needs to be extensively validated for the flow through pump components so that pump designers have the confidence to use it. The present work is focused on steady-state component

analysis to validate the algorithm with a one-equation turbulence model and to demonstrate the code capability. For the pump components, such as an inducer and a radial impeller, the steady flow assumption is valid without the diffuser and inlet guide vanes. The progress in unsteady pump flows will be reported in future. A similar effort can be seen in the activities of the other members of MSFC pump stage technology team.⁶⁻⁸ Their formulations are based on a pressure based method and the current formulation is based on a pseudocompressibility method.

The numerical solution of the incompressible Navier-Stokes equations requires special attention in order to satisfy the divergence-free constraint on the velocity field because the incompressible formulation does not yield the pressure field explicitly from the equation of state or through the continuity equation. One way to avoid the numerical difficulty originated by the elliptic nature of the problem is to use a pseudocompressibility method. With the pseudocompressibility method, the elliptic-parabolic type equations are transformed into hyperbolic-parabolic type equations. Well established solution algorithms developed for compressible flows can be utilized to solve the resulting equations. Steger and Kutler⁹ employed an alternating direction implicit scheme into Chorin's¹⁰ pseudocompressibility method. This formulation was extended to three-dimensional generalized coordinates by Kwak and Chang.^{11,12} Recently, a three-dimensional incompressible Navier-Stokes solver¹³ (INS3D-UP) using upwind differencing and Gauss-Seidel line relaxation scheme was developed in order to have a robust and fast converging scheme. The flow over single and multi-element airfoils was efficiently simulated by using this algorithm.¹⁴ A time accurate formulation of the algorithm is implemented for incompressible flows through artificial heart devices with moving boundaries.¹⁵ The present study is the continuation of the validation effort for the turbulent flow in rotating machinery in steadily rotating frame of reference.

In the next section, the governing equations and the method of solution are summarized. Following that is a presentation of the computed results obtained from the current approach.

Governing Equations and Method of Solution

The pseudocompressibility algorithm introduces a time derivative of the pressure term into the continuity equation. The resulting incompressible Navier-Stokes equations can be written in a generalized curvilinear coordinate system (ξ, η, ζ) as follows

$$\frac{\partial Q}{\partial \tau} + \frac{\partial}{\partial \xi}(E - E_v) + \frac{\partial}{\partial \eta}(F - F_v) + \frac{\partial}{\partial \zeta}(G - G_v) = S \quad (1)$$

where Q , and the convective flux vectors E, F, G are

$$Q = \frac{1}{J} \begin{bmatrix} p \\ u \\ v \\ w \end{bmatrix}$$

$$\begin{aligned}
E &= \frac{1}{J} \begin{bmatrix} \beta U \\ \xi_x p + uU + \xi_t u \\ \xi_y p + vU + \xi_t v \\ \xi_z p + wU + \xi_t w \end{bmatrix} \\
F &= \frac{1}{J} \begin{bmatrix} \beta V \\ \eta_x p + uV + \eta_t u \\ \eta_y p + vV + \eta_t v \\ \eta_z p + wV + \eta_t w \end{bmatrix} \\
G &= \frac{1}{J} \begin{bmatrix} \beta W \\ \zeta_x p + uW + \zeta_t u \\ \zeta_y p + vW + \zeta_t v \\ \zeta_z p + wW + \zeta_t w \end{bmatrix}
\end{aligned}$$

Here J , β , p , u , v , and w denote the Jacobian of transformation, the pseudocompressibility coefficient, pressure, and cartesian velocity components, respectively. The contravariant velocity components U , V , and W are defined as

$$\begin{aligned}
U &= \xi_x u + \xi_y v + \xi_z w \\
V &= \eta_x u + \eta_y v + \eta_z w \\
W &= \zeta_x u + \zeta_y v + \zeta_z w
\end{aligned}$$

The viscous fluxes, E_v , F_v , and G_v , are given by

$$\begin{aligned}
\hat{E}_v &= \frac{1}{ReJ} \begin{bmatrix} (\nabla \xi \cdot \nabla \xi)u_\xi + (\nabla \xi \cdot \nabla \eta)u_\eta + (\nabla \xi \cdot \nabla \zeta)u_\zeta \\ (\nabla \xi \cdot \nabla \xi)v_\xi + (\nabla \xi \cdot \nabla \eta)v_\eta + (\nabla \xi \cdot \nabla \zeta)v_\zeta \\ (\nabla \xi \cdot \nabla \xi)w_\xi + (\nabla \xi \cdot \nabla \eta)w_\eta + (\nabla \xi \cdot \nabla \zeta)w_\zeta \end{bmatrix} \\
\hat{F}_v &= \frac{1}{ReJ} \begin{bmatrix} (\nabla \eta \cdot \nabla \xi)u_\xi + (\nabla \eta \cdot \nabla \eta)u_\eta + (\nabla \eta \cdot \nabla \zeta)u_\zeta \\ (\nabla \eta \cdot \nabla \xi)v_\xi + (\nabla \eta \cdot \nabla \eta)v_\eta + (\nabla \eta \cdot \nabla \zeta)v_\zeta \\ (\nabla \eta \cdot \nabla \xi)w_\xi + (\nabla \eta \cdot \nabla \eta)w_\eta + (\nabla \eta \cdot \nabla \zeta)w_\zeta \end{bmatrix} \\
\hat{G}_v &= \frac{1}{ReJ} \begin{bmatrix} (\nabla \zeta \cdot \nabla \xi)u_\xi + (\nabla \zeta \cdot \nabla \eta)u_\eta + (\nabla \zeta \cdot \nabla \zeta)u_\zeta \\ (\nabla \zeta \cdot \nabla \xi)v_\xi + (\nabla \zeta \cdot \nabla \eta)v_\eta + (\nabla \zeta \cdot \nabla \zeta)v_\zeta \\ (\nabla \zeta \cdot \nabla \xi)w_\xi + (\nabla \zeta \cdot \nabla \eta)w_\eta + (\nabla \zeta \cdot \nabla \zeta)w_\zeta \end{bmatrix}
\end{aligned}$$

where Re is the Reynolds number.

When the equations are solved in steadily rotating reference frames, the centrifugal force and the Coriolis force terms are added to the equation of motion as source terms. If the relative reference frame is moving around x -axis, the source term S is given by

$$S = \begin{bmatrix} 0 \\ 0 \\ \Omega(\Omega y + 2w) \\ \Omega(\Omega z - 2v) \end{bmatrix}$$

where Ω is the rotational speed. Both the viscous and source terms are treated implicitly in the numerical formulation. Relative velocity components are written in terms of

absolute velocity components u_a , v_a , and w_a as

$$\begin{aligned} u &= u_a \\ v &= v_a + \Omega z \\ w &= w_a - \Omega y \end{aligned}$$

In the steady-state formulation, the time derivatives are differenced using the Euler backward formula. The equations are solved iteratively in pseudo-time until the solution converges to a steady state. Central differencing is used to compute the viscous flux derivatives and third-order upwind differencing is employed to compute the convective flux derivatives. Chakravarthy outlines a class of high-accuracy flux-differencing schemes for the compressible flow equations.¹⁶ Following Chakravarthy's third-order scheme, a fifth-order-accurate, upwind-biased stencil was derived by Rai.³ The upwind differencing used here is an implementation of those efforts for the incompressible Navier-Stokes equations. For the computations presented in this report, third-order flux-differencing scheme is used.

An implicit, delta-law form approximation to Eq.(1) after linearization in time and the use of approximate Jacobians of the flux differences results in a seven-block diagonal matrix equation written as

$$\begin{aligned} \bar{B}\delta Q_{i-1,j,k} + \bar{A}\delta Q_{i,j,k} + \bar{C}\delta Q_{i+1,j,k} + \bar{D}\delta Q_{i,j-1,k} \\ + \bar{E}\delta Q_{i,j+1,k} + \bar{F}\delta Q_{i,j,k-1} + \bar{G}\delta Q_{i,j,k+1} = R.H.S. \end{aligned} \quad (2)$$

where $\delta Q = Q^{n+1} - Q^n$ and $\bar{A}, \bar{B}, \bar{C}, \bar{D}, \bar{E}, \bar{F}$, and \bar{G} are 4 x 4 block diagonals.

The Gauss-Seidel line relaxation scheme, which was successfully employed by MacCormack¹⁷, is used to solve this matrix equation. In Eq. (2), the right-hand-side term is computed and stored for the entire domain. In the present study, the line relaxation procedure is composed of three stages; each stage involves a block tridiagonal inversion in one direction. Fig. 1 shows the block tridiagonal inversion lines and the Gauss-Seidel sweep planes for the three directions. In the first stage, δQ is solved line-by-line in one direction. Before the block tridiagonal equation is solved, off-tridiagonal terms are multiplied by the current value of δQ and are shifted over to the right-hand-side of the equation. In other words, Eq. (2) is solved by performing a block tridiagonal inversion in the ξ -direction, and Gauss-Seidel sweeps in the η -, and ζ -directions. The second stage is to solve the block tridiagonal terms in the η -direction, and to perform backward and forward sweeps in the ζ - and ξ -directions. The same procedure is repeated in the third stage by inverting the block tridiagonal matrix in the ζ -direction, and treating the off-diagonal terms for the ξ -, and η -directions in Gauss-Seidel fashion. After the first sweep is completed for the entire domain, a backward sweep is started in the opposite direction. One forward sweep and one backward sweep for each computational direction are sufficient for most problems, but the number of sweeps can be increased.

Implicit boundary conditions are used at all of the boundaries except the zonal interface boundaries; zonal interface boundaries are updated quasi-implicitly which is very suitable for the line-relaxation scheme. The change in the dependent variables for one time-step is passed during line-relaxation sweeping from one zone to another.

No-slip boundary conditions are imposed at the solid stationary wall. The pressure boundary condition is specified such that the pressure gradient normal to the wall is zero. At the inflow and outflow boundaries, characteristic boundary conditions are employed implicitly. It is assumed that the effect of viscous terms at the boundaries is negligible. Also, the characteristic equations are approximated in one-dimensional space. The primitive variables which are needed at the boundaries are the pressure p , and velocity components u, v, w . The number of positive and negative eigenvalues of the Jacobian matrix of the convective flux determines how many variables should be specified at the boundaries. If the flow is in the positive ξ -direction, then there will be three characteristic waves travelling downstream and one characteristic wave travelling upstream. The exit boundary receives the information about the three variables via the characteristics travelling from the interior of the domain. Hence, only one variable is specified at the outflow boundary. However, the inflow boundary receives only one characteristic travelling from the interior region. Therefore, three variables are specified at the inflow boundary. For the calculations presented in this report, u, v and w velocities were specified at the inflow and static pressure was specified at the outflow. Details of the numerical method are given in Ref. 13.

The present calculations use the one-equation turbulence model developed by Baldwin and Barth.¹⁸ The transport equation for the turbulent Reynolds number is derived from a simplified form of the standard $k - \epsilon$ model equations. The model is relatively easy to implement because there is no need to define an algebraic length scale. The formulation and code issues can be found in Ref. 18. The transport equation is also solved using a Gauss-Seidel type line relaxation scheme.

Computed Results

In this section, the inducer results are presented to validate the solution method. The impeller results demonstrate how the computational procedure can be used in the design analysis. In inducer and impeller calculations, the flow is simulated in one blade passage and the flow periodicity is used for the adjacent blade passages.

Pump Inducer

The flowfield through a turbopump inducer is solved as a benchmark problem for turbomachinery applications. A pump inducer geometry with a high flow coefficient as shown in Fig. 2 was developed and experimentally studied by Rocketdyne division of Rockwell International. An inducer which provides a sufficient pressure rise to the flow in order to prevent the cavitation on impeller blades is a crucial element of a rocket engine pump. The design flow of the Rocketdyne inducer is 2236 gal/min with a design speed of 3600 rpm. The tip diameter of the inducer is six inches. In the computational study, tip-leakage effects are included with a tip clearance of 0.008 inches. The problem was nondimensionalized with a reference length of one inch and the average inflow velocity of 339.6 in/sec. The Reynolds number for this calculation was 191,800. The upstream section of the inducer was taken as a 10 inch long straight channel as shown

in Fig. 2. The inducer grid was generated for one blade passage which is one-sixth of the cross-section of the tube. An H-H grid topology with dimensions of $187 \times 27 \times 35$ was used. H-type surface grid was generated for each surface by using an elliptic grid generator. The interior region of the three-dimensional grid was filled by using an algebraic solver coupled with an elliptic smoother. The bull-nose of the inducer was treated as a rotating wall and the cavity section was neglected. However, this region can be included by using an additional zone. Periodic boundary conditions were used at the end points in the rotational direction. The solution was considered converged when the maximum residual dropped at least five orders of magnitude. The convergence history is shown in Fig. 3. Computer time required per grid point per iteration was about 1.5×10^{-4} sec. The total computer time for this calculations was about 4-6 Cray-YMP hours. The same calculations were performed on an SGI-Indigo workstations, and the turnaround time was about 4-5 days.

The surface of the inducer hub and blades is colored by nondimensionalized pressure in Fig. 4. The pressure is nondimensionalized by ρV^2 where ρ is the density and V is the average inflow velocity. The pressure gradient across the blades due to the action of centrifugal force and the pressure rise from inflow to outflow are shown. Fig. 5 shows the particle traces colored by relative velocity magnitude. The particles were released near the hub, the blade suction side, and the tip regions, then the traces were calculated from the relative velocity field. Near the hub, the particles rise up in the boundary-layer and move from the pressure side to the suction side of the blade. The swirling motion of the particles indicate a secondary flow region near the hub. The particles released near the suction side of the blade indicate a radial velocity component inside the blade boundary layer, because low energy fluid is controlled by centrifugal force. The particles tend to flow from the hub suction side to tip suction side of the blade. The particles near the casing show an opposite trend than the ones near the hub. Since the casing has counterrotating wheel speed in the relative frame of reference, the particles move from the suction side to the pressure side.

Figures 6-a through 6-d illustrate the cross-sections where the computational results are compared with the experimental measurements. The positions of planes A, B, C, and D in x -direction (streamwise direction) are shown in Fig. 7. At each plane, the results are presented at every other circular arc shown in Fig. 6. Relative total velocities and relative flow angles obtained from the current computation are compared with experimental data. The total velocity is defined to include only the axial and tangential velocity components because the radial velocity component is not available experimentally. The flow angle is computed as the angle between the axial velocity and the total velocity. Figs. 8 through 11 show relative total velocities and relative flow angles as a function of circumferential angle in degrees in planes A, B, C, and D, respectively. The circumferential angle increases from the suction side to the pressure side of the blade. The symbols represent the experimental measurements and solid lines represent the numerical results. The comparison of computations and experiment near the leading edge region (plane A) is good all the way from the hub to the tip region. Both velocities and flow angles show the same trend as observed in the flow measurements. Inside the blade passage (plane B), numerical results compare fairly well with experimental data. Figs. 9-a and 9-b indicate the biggest discrepancy near

the hub region. The computational study underpredicts the axial velocities near the suction side of the hub secondary flow region. This may be a result of the relatively coarse grid used for the boundary layer. However, the core and the tip region show very good agreement with the measurements. As we move downstream, the error at the hub section decreases substantially as seen in Figs. 10-a and 10-b ($R = 1.803$). The core region of plane C also shows a good trend compared with the measurements. However, a 5-8 % error in the velocities is observed near the casing wall of plane C. Computational results overpredict the wake strength at the suction side of $R = 2.95$. Finally, the results in the mixing region (plane D) are compared with the measurements in Figs. 11-a and 11-b. The location of the wake in the core region indicates a 5 to 10 degree difference between the numerical results and the measurements ($R = 2.221$ and $R = 2.587$). This might be due to clocking error between the computational grid and the locations of the measurements during the postprocessing. In planes A,B, and C, the suction side and the pressure side have borders with the blades. Therefore, there should not be any error in the postprocessing. In plane D, it is assumed that the suction side starts at the same angle of the blade trailing edge. Since the computational grid does not follow the same circumferential angle with the blade trailing edge downstream, it is possible to have an order of a couple of degrees clocking difference between computational and experimental suction sides. The structure of the internal turbulent flow in the present configuration is quite complicated. The comparison shows that the solution algorithm does a reasonably good job. The existing solution procedure can be applied to a similar configuration in off-design conditions. Such a numerical study could potentially predict cases where the inducer may suffer from massive separation resulting in a blocked fuel supply. This provides the designer a safe operating envelope of a particular inducer. This is the future research area of this study which can be used in the pre-design and post-design engineering tool in challenging turbomachinery applications.

Pump Impeller

The current procedure was applied in a flow analysis inside an advanced pump impeller geometry to verify the design. In addition to the present computations, impeller analyses were performed by other members of the NASA-MSFC Pump Consortium Team. A good trend was obtained between all CFD analyses, and the results were presented at the Tenth Workshop for CFD Applications in Rocket Propulsion.¹⁹ A computer generated surface of the impeller blades is illustrated in Fig. 12. The impeller design flow is 1,205 gal/min with a design speed of 6,322 rpm. The problem was non-dimensionalized with a reference length of one inch and average inflow velocity of 284 in/sec. The Reynolds Number for this calculation was 181,273 per inch. A zonal grid method was employed for this computation due to the geometric complexity. Fig. 13 shows the computational grid near the hub region of the impeller. The domain is divided into four zones with dimensions of 89 x 52 x 33, 75 x 26 x 33, 75 x 26 x 33, and 41 x 76 x 33 respectively. Zone 1 starts from the inflow plane and ends at the leading edge of the partial blade. The region between the suction side of the full blade and the pressure side of the partial blade is filled by Zone 2. Zone 3 is the region between the suction side of the partial blade and the pressure side of the full blade. Zone 4 occupies

downstream of the discharge plane of the impeller. At the zonal interfaces, grid points were matched one-to-one. For all zones, an H-H type grid topology was used.

In Zone 1 and Zone 4, the flow periodicity was imposed at the boundaries in the rotational direction. Tangential and meridional velocities as obtained from the designers were specified at the inflow boundary. The initial flow was specified to be fully rotated with meridional velocities equal to unity. The solution was considered converged when maximum residual was dropped below 1.0^{-5} , which was obtained in less than 1500 iterations. The computer time required for each impeller analysis was about 20 Cray-YMP hours.

Initially, the flow through baseline and optimized geometries were simulated at design flow rate. The overall efficiency and head coefficient of the baseline impeller are 94 percent and 0.66, respectively. The overall efficiency and head coefficient for optimized impeller are predicted as 98 percent and .636, respectively. The overall relative discharge flow angle is predicted as 25 degree for the baseline impeller and as 18 degree for the optimized impeller. The computational results indicate that efficiency parameters are improved from the baseline to optimized impeller. For these calculations, the hub and shroud walls downstream of the impeller exit were considered as stationary walls. In order to have code-to-code comparison with other analyses, slip downstream boundary conditions were used in further computations. The results with slip and non-slip boundary conditions will also show the effect of downstream conditions. With slip boundary conditions, both design and off-design conditions were simulated. Fig. 14 shows the meridional velocity distribution at the impeller discharge. A relative x -distance is measured from the shroud to the hub, where $x = 1.0$ is the hub. The meridional velocities, CM , were integrated along a radial strip for each constant x -position and they were non-dimensionalized by the wheel tip speed of 249.5 ft/sec. In Fig. 14, the dotted line with diamonds represents CM distributions for the design flow with non-slip stationary downstream boundary conditions. The solid line denotes the CM distributions for the design flow with slip downstream boundary conditions. The effect of downstream boundary conditions can be seen by comparing the solid line and the dotted line in Fig. 14. When slip downstream boundary conditions are used, the flow is pumped near hub and shroud regions, and the velocity profile is flattened in the core region. The meridional velocity distributions for various off-design conditions were also plotted in Fig. 14. The impeller rotational speed was kept the same as design speed and the mass flow was controlled in order to reach off-design conditions. For all off-design cases, slip downstream boundary conditions were used. The dashed line with filled squares shows CM distributions for 120% of design flow. The trend in CM for 120% of design flow is very similar to the design flow case. However, the 80% and 60% cases have a trend opposite of the design case in that the meridional velocities are smaller near the shroud and are larger near the hub region. In Fig. 15, relative flow angles were plotted for design and off-design cases. The design case indicates a nearly constant relative flow angle distribution at the discharge of the impeller. For higher flow rate, relative flow angles were increased near the shroud and they were decreased near the hub. Conversely, the lower flow rates indicate low flow angles near the shroud and high flow angles near the hub. Fig. 16 plots meridional velocity profiles versus relative angle at the impeller discharge for different x -locations. The relative angle is mea-

sured from the suction side of the full blade to the pressure side of the full blade. The velocities increase in magnitude from the suction side of the full blade to the pressure side of the partial blade. There is a sudden jump because of the presence of the partial blade. From the suction side of the partial blade to the pressure side of the full blade, the meridional velocities increase again. The lowest meridional velocities are seen near the shroud on the suction sides of the blades. Impeller discharge distributions, such as flow angle, velocity, etc., at various operating conditions are important for turbopump designers because they affect the diffuser blade loading. It is believed that there will be an iterative design improvement process between designers and numerical analysts in impeller-diffuser configurations.

Figure 17-a shows the particle traces released near the shroud region for 120%, 100%, and 80% of the design flow cases. For all cases, a secondary flow region is observed near the suction side of the partial blade. In 80% of design flow, particles moved from the shroud to the hub direction as they were in the recirculation region. Fig. 17-b illustrates the particle traces released near the hub region for high, design, and low flow rates. The particles near the hub region move from the pressure side of the blades toward the suction side of the blades. The flow is also separated near the suction side of the trailing edge of the full blade. Since the higher flow rates yield higher meridional velocities near the hub, this separation region is smaller. Conversely, the particles leave the full blade suction side at early stage for the low flow rate. Figs. 18-a through 18-d show the velocity vectors on the cross-section plane, which is downstream of the full blade leading edge, for 100%, 120%, 80% and 60% of design flow, respectively. Relative velocity vectors for all cases indicate that there is a back flow near the shroud of impeller. Also a secondary flow region can be seen near the corner of pressure side blade and the shroud. For high flow rates, the secondary flow region is not so strong as seen in Fig. 18-b. When the flow rate is decreased (Figs. 18-c and 18-d) the backflow near the shroud increases and tends to pre-swirl. In 60% of design flow case, this pre-swirl becomes stronger. As mentioned above, one of the concerns at the design stage was the distortion at the impeller exit. For this purpose, the relative velocity vectors at the discharge plane are plotted in Fig. 19-a. The suction side of the full blade region and the suction side of the partial blade region are magnified in Figs. 19-b, and 19-c, respectively. The full blade suction side indicates a stronger flow distortion than the partial blade suction side. Computed results with slip boundary conditions indicate that the flow split between full blades and partial blades is .44/.56 for design flow. The 80% and 120% flow cases do not show a significant change in the flow split. For 60% of design flow, the flow split is computed to be .37/.63.

Flow through the SSME fuel pump impeller has been simulated using the present approach. These results will be reported when the experimental data is available.

Concluding Remarks

An efficient and robust solution procedure for 3-D pump component analyses has been presented. The technique solves the viscous incompressible Navier-Stokes equations with source terms in a steadily rotating reference frame. The method of pseudo-compressibility with higher-order accurate upwind differencing and a Gauss-Seidel line

relaxation scheme are utilized. The flow through a pump inducer and an impeller have been successfully simulated. Inducer results in the form of relative total velocity and relative flow angle in four planes are presented. Numerical results from a one-equation Baldwin-Barth turbulence model compare fairly well with experimental data. Impeller analyses for design and off-design conditions demonstrate the possible opportunities for CFD to be used in the design stage of the pump components. Investigation of other turbulence models for the pump flows, grid resolution study, unsteady flows, and further validation cases will be the focus of future study.

References

- ¹ Garcia, R., Jacson, E.D., and Schutzenhofer, L.A., "A Summary of the Activities of the NASA/MSFC Pump Stage Technology Team," Proceedings of the Fourth International Symposium on Transport Phenomena and Dynamics of Rotating Machinery, April 5-8 1992, Honolulu, Hawaii.
- ² Garcia, R., McConnaughey, P., and Eastland, A., "Activities of MSFC Pump Stage Technology Team," AIAA Paper No. 92-3232, 1992.
- ³ Rai, M. M. "Unsteady Three-Dimensional Navier-Stokes Simulations of Turbine Rotor-Stator Interaction," AIAA Paper No. 87-2058, 1987.
- ⁴ Giles, M. B. "Generalized Conservation Cells for Finite Volume Calculations," AIAA Paper No. 87-1118, 1987.
- ⁵ Giles, M. B. "Stator/Rotor Interaction in a Transonic Turbine," AIAA Paper No. 88-3093, 1988.
- ⁶ Hah, C., Brayns, A.C., Moussa, Z., and Tomsho, M. E., "Application of Viscous Flow Computations for Aerodynamic Performance of a Backswept Impeller at Viscous Operating Conditions," J. of Turbomachinery, Trans. ASME, Vol. 110, pp. 303-311, July 1988.
- ⁷ Chen, Y. S., "Compressible and Incompressible Flow Computations with a Pressure Based Method," AIAA Paper No. 89-0286, 1989.
- ⁸ Chen, W. C., Pruger, G., Chen, D., and Eastland, A., "On the Use of a Three-Dimensional Navier-Stokes Solver for Rocket Pump Impeller Design," AIAA Paper No. 92-3223, 1992.
- ⁹ Steger, J. L., Kutler, P., "Implicit Finite-Difference Procedures for the Computation of Vortex Wakes," *AIAA Journal*, Vol 15, no. 4, pp. 581-590, 1977.
- ¹⁰ Chorin, A., J., "A Numerical Method for Solving Incompressible Viscous Flow Problems," *Journal of Computational Physics*, Vol. 2, pp. 12-26, 1967
- ¹¹ Kwak, D., Chang, J. L C., Shanks, S. P., and Chakravarthy, S., "A Three-Dimensional Incompressible Navier-Stokes Flow Solver Using Primitive Variables," *AIAA Journal*, Vol 24, no. 3, pp. 390-396, 1977.
- ¹² Chang, J., Kwak, D., Rogers, S. E., and Yang, R.-J., "Numerical Simulation Methods of Incompressible Flows and an Application to the Space Shuttle Main Engine," *Int. J. Num. Meth. in Fluids*, Vol 8, pp. 1241-1268, 1988.
- ¹³ Rogers, S. E., Kwak, D. and Kiris, C., "Numerical Solution of the Incompressible Navier-Stokes Equations for Steady and Time-Dependent Problems," *AIAA Journal*, Vol 29, No 4, pp. 603-610, 1991.

- ¹⁴ Rogers, S. E., Wiltberger, N. L., and Kwak, D. "Efficient Simulation of Incompressible Viscous Flow Over Single and Multi-Element Airfoils," AIAA Paper No. 92-0405, 1992.
- ¹⁵ Kiris, C., Rogers, S. E., Kwak, D. and Chang, I. "Computation of Incompressible Viscous Flows with Moving Boundaries," Proc. Intl. Symposium on Biofluidynamics, July 6-12, 1991.
- ¹⁶ Chakravarthy, S. R., Osher, S., "A New Class of High Accuracy TVD Schemes for Hyperbolic Conservation Laws," AIAA Paper No. 85-0363, 1985.
- ¹⁷ MacCormack, R., W., "Current Status of Numerical Solutions of the Navier-Stokes Equations," AIAA Paper No. 85-0032, 1985.
- ¹⁸ Baldwin, B., S. and Barth, T., J., "A One-Equation Turbulence Transport Model for High Reynolds Number Wall-Bounded Flows," AIAA Paper No. 91-0610, 1991.
- ¹⁹ Garcia, R., and Williams, R., W., "A Status of the Activities of the MSFC Pump Stage Technology Team," Tenth Workshop for CFD Applications in Rocket Propulsion, April 28-30 1992, NASA-MSFC.

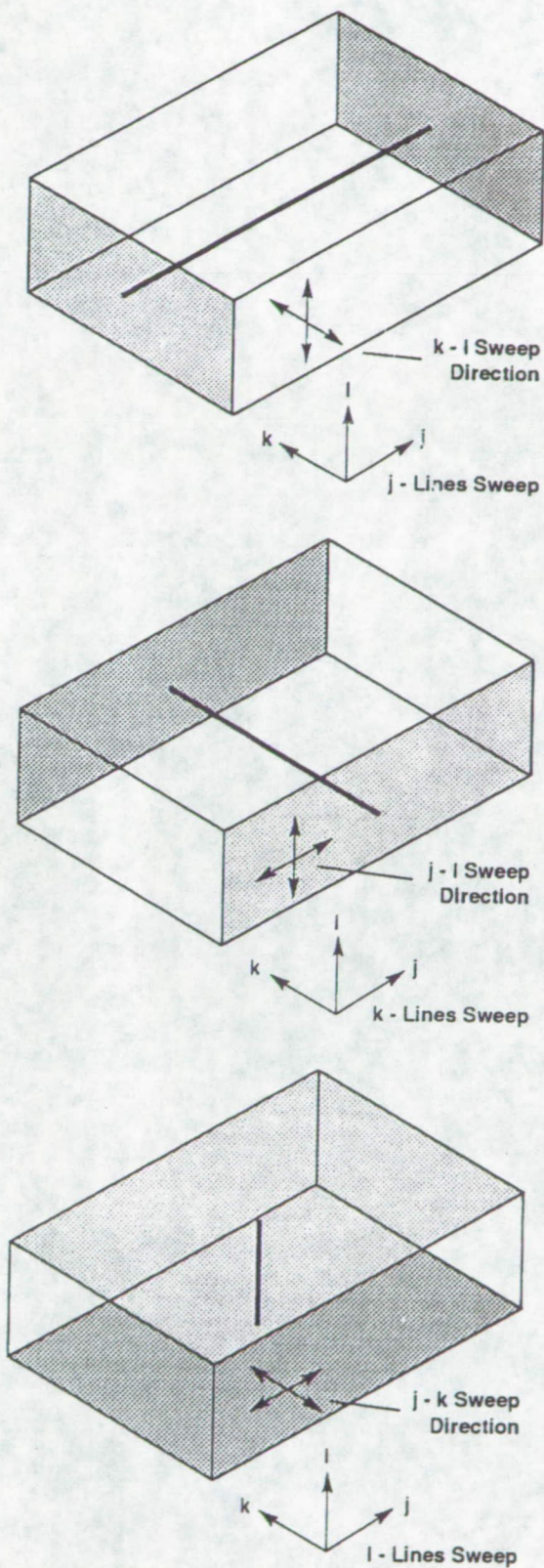


Fig. 1. Gauss-Seidel sweep directions.



Fig. 2. Rocketdyne turbopump inducer configuration.

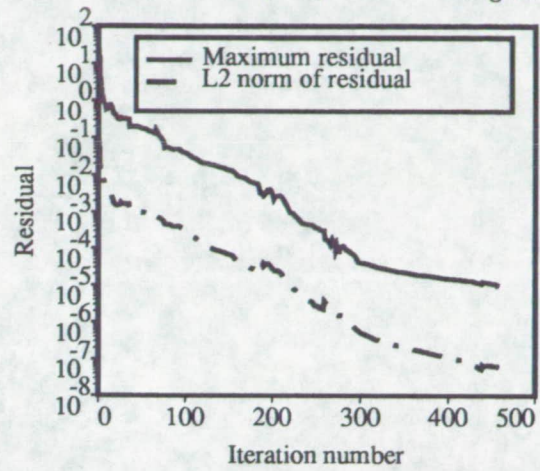


Fig. 3. Convergence history for inducer calculations.

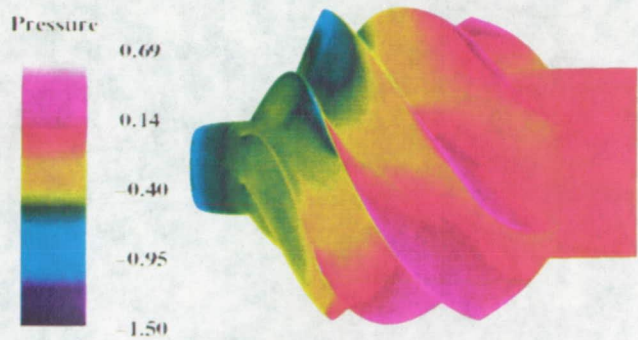


Fig. 4. Surface pressure of the pump inducer.



Fig. 5. Particle traces colored by relative total velocity magnitude.

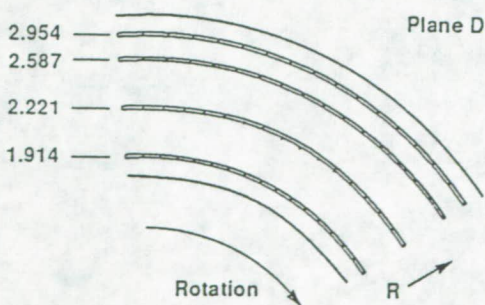
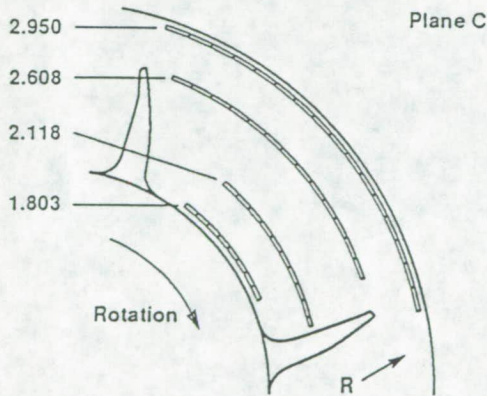
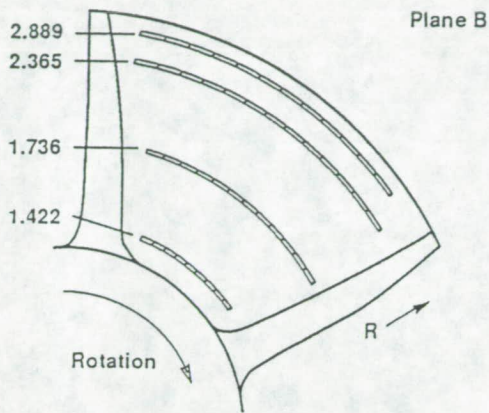
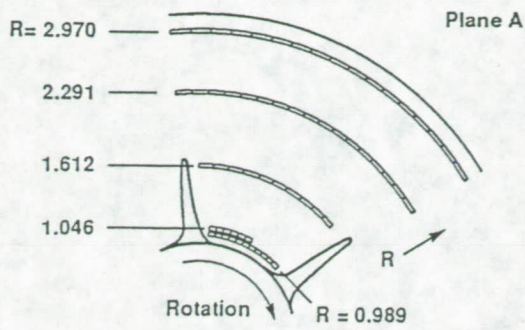


Fig. 6. Schematic representation of circular arcs where the results are compared with experimental data in a) plane A; b) plane B; c) plane C; d) plane D.

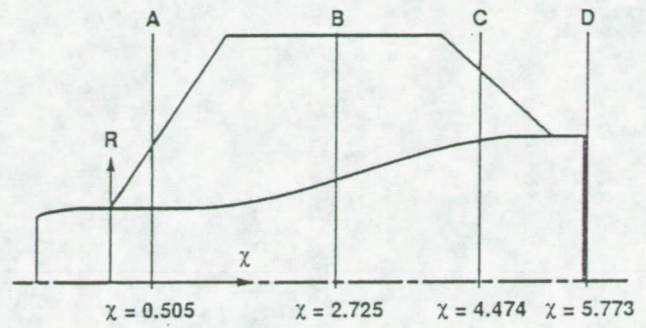


Fig. 7. Schematic representation of planes where experimental data is available

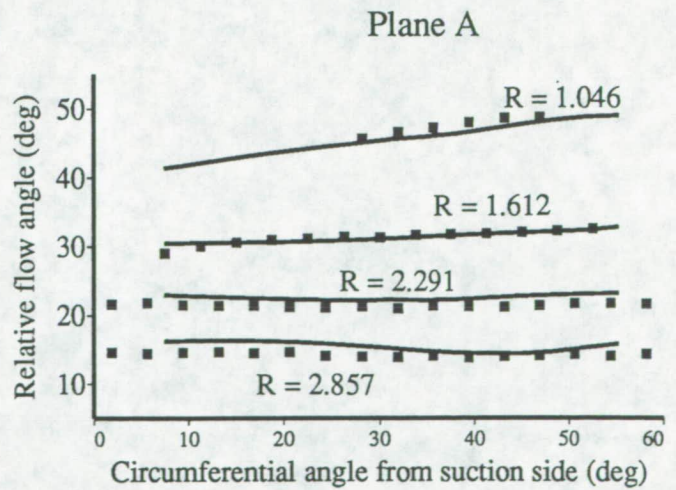
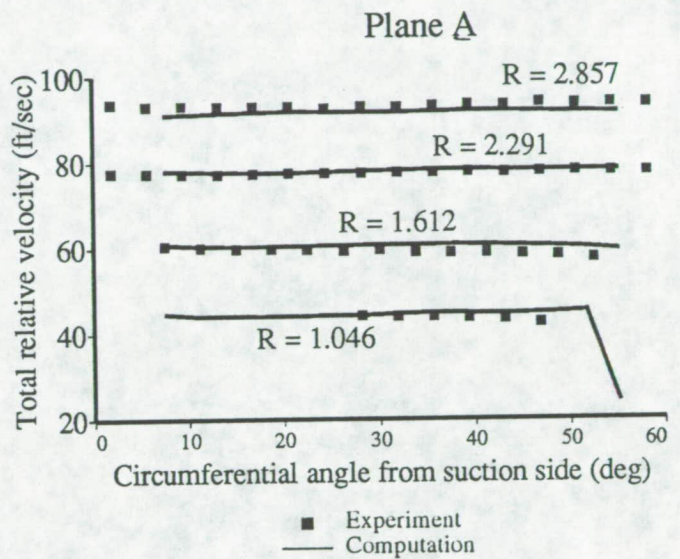


Fig. 8. Comparison of relative total velocity and relative flow angle in plane A.

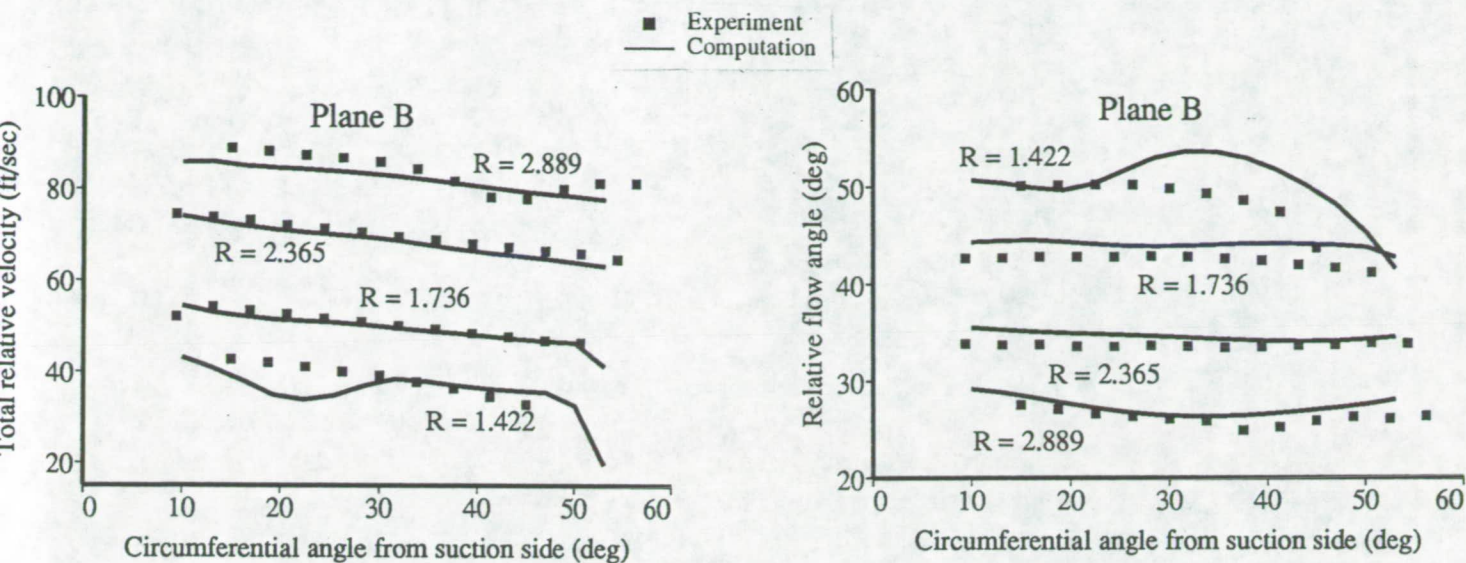


Fig. 9. Comparison of relative total velocity and relative flow angle in plane B.

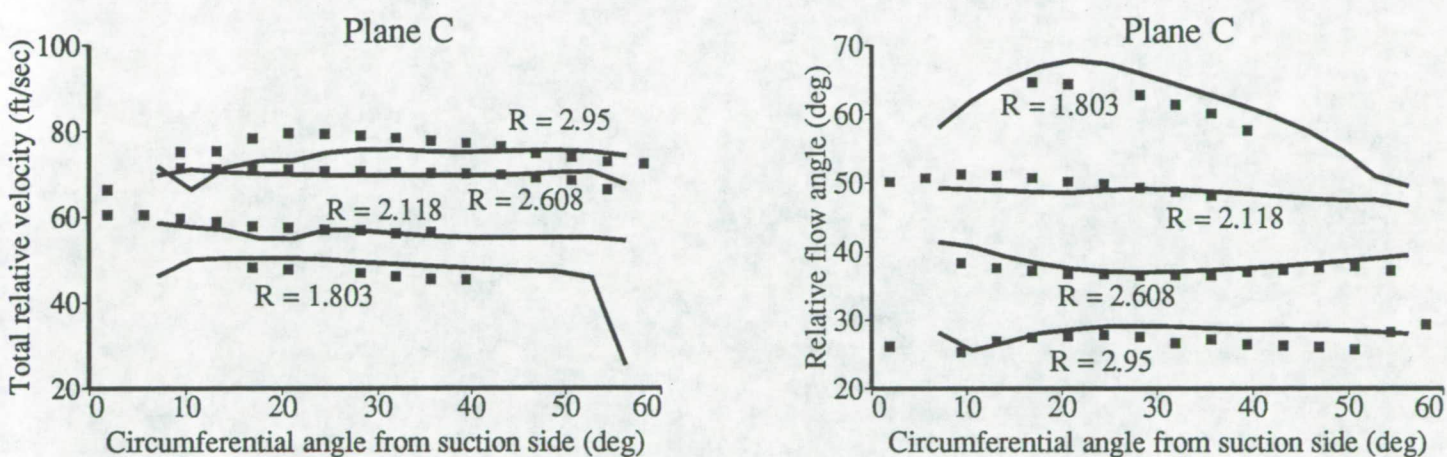


Fig. 10. Comparison of relative total velocity and relative flow angle in plane C.

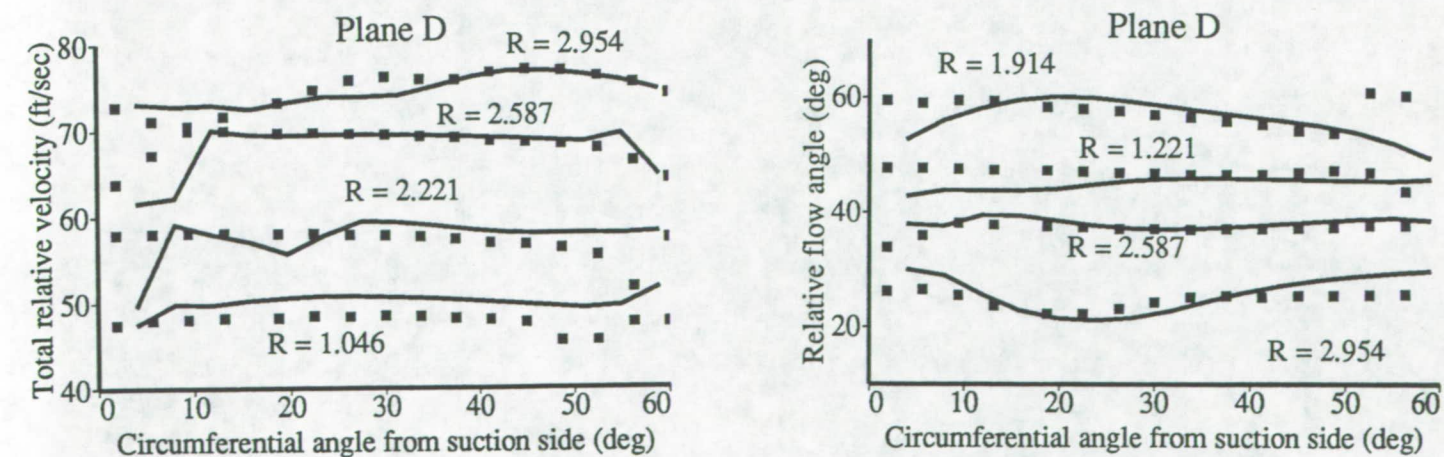


Fig. 11. Comparison of relative total velocity and relative flow angle in plane D.

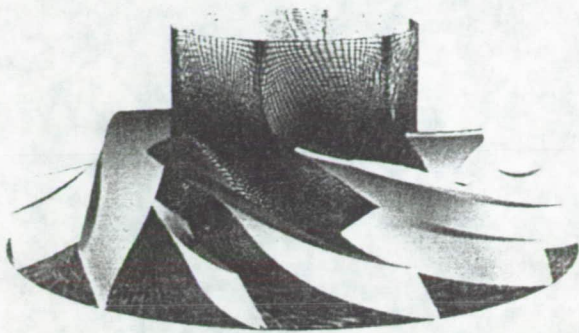


Fig. 12. Advanced pump impeller geometry.

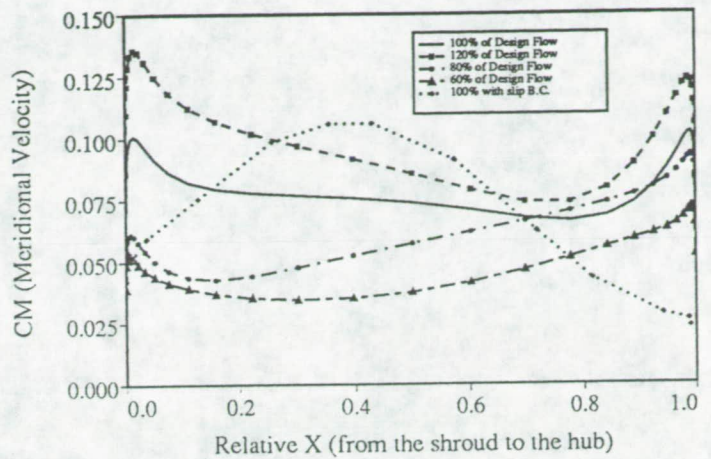


Fig. 14. Impeller exit meridional velocity distributions.

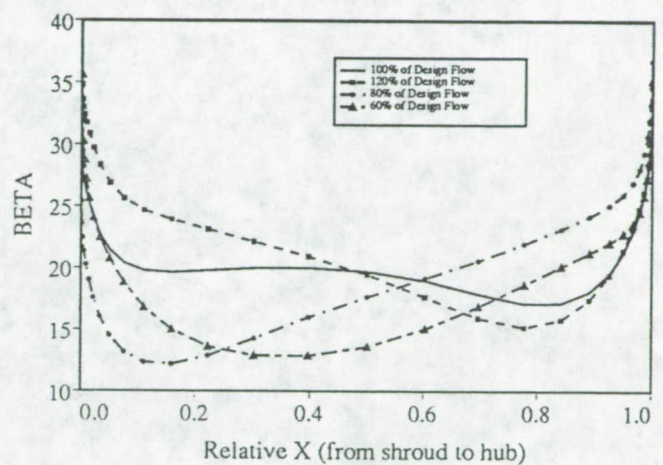
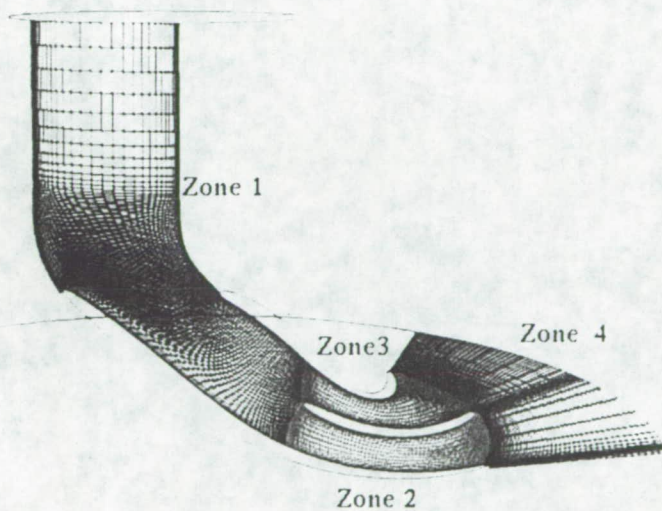


Fig. 15. Impeller exit relative flow angle distributions.



Fig. 13. Computational grid used in the impeller analysis.

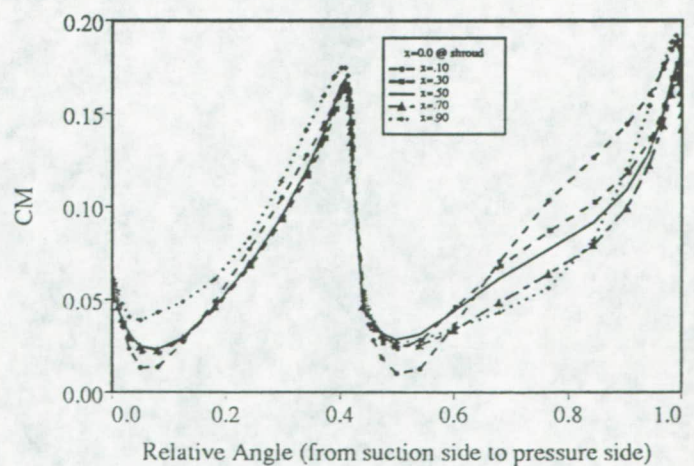


Fig. 16. Impeller exit meridional velocity profiles at several x -locations from the shroud to the hub.

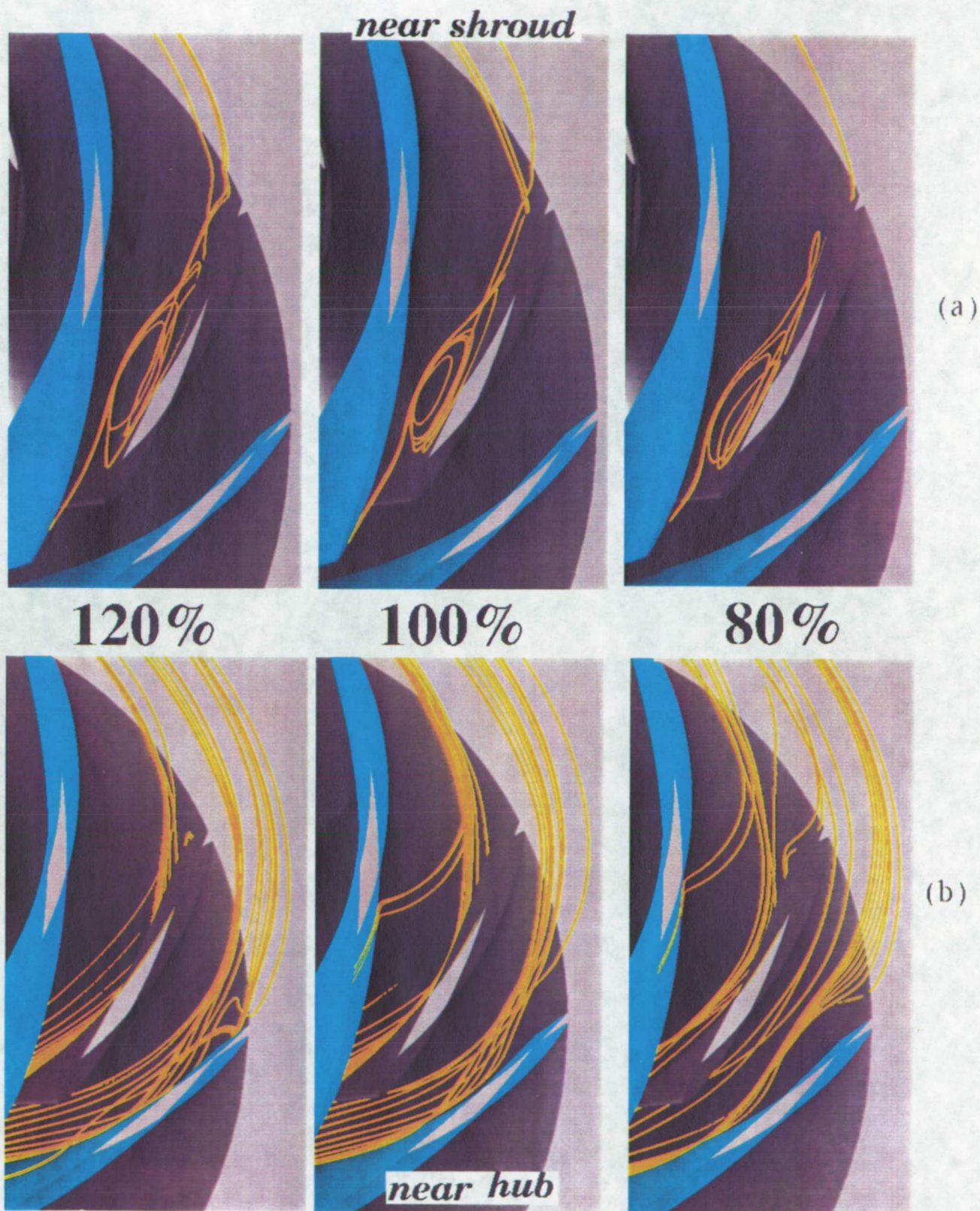


Fig. 17. Particle traces released near the shroud and near the hub region for design and off-design cases.

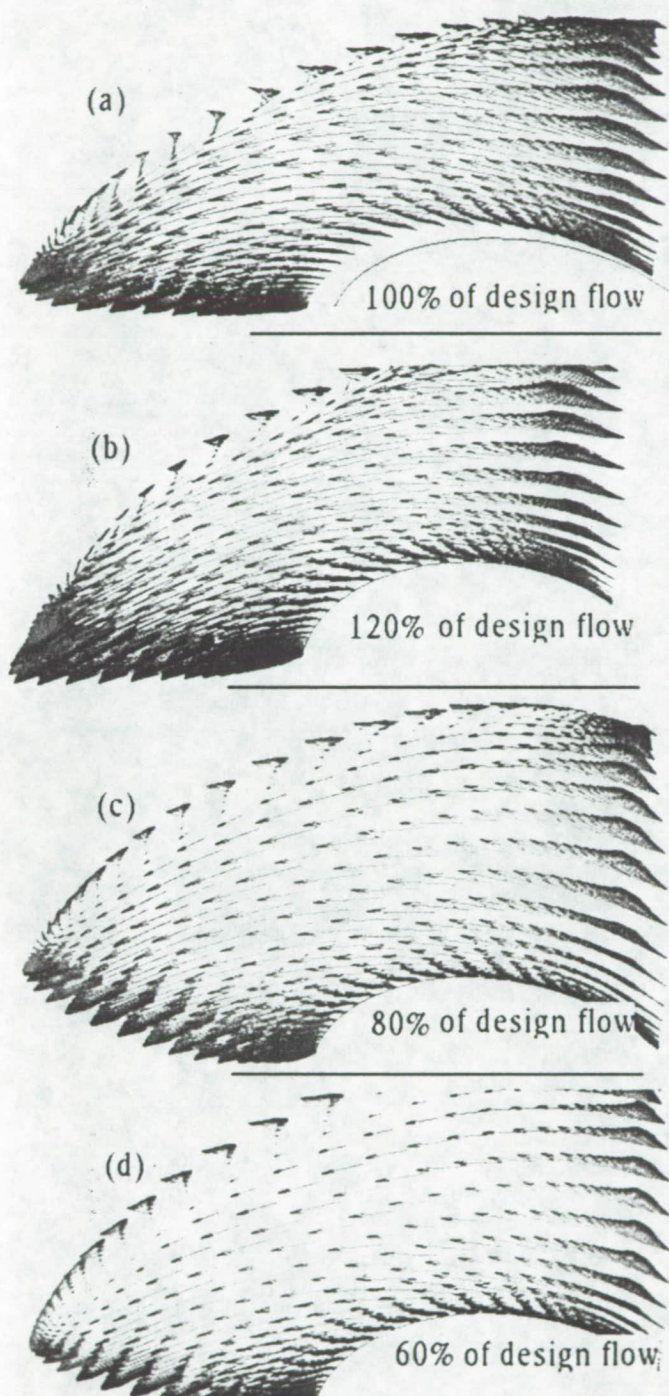


Fig. 18. Relative velocity vectors at impeller inlet for 100%, 120%, 80% and 60% of design flows.

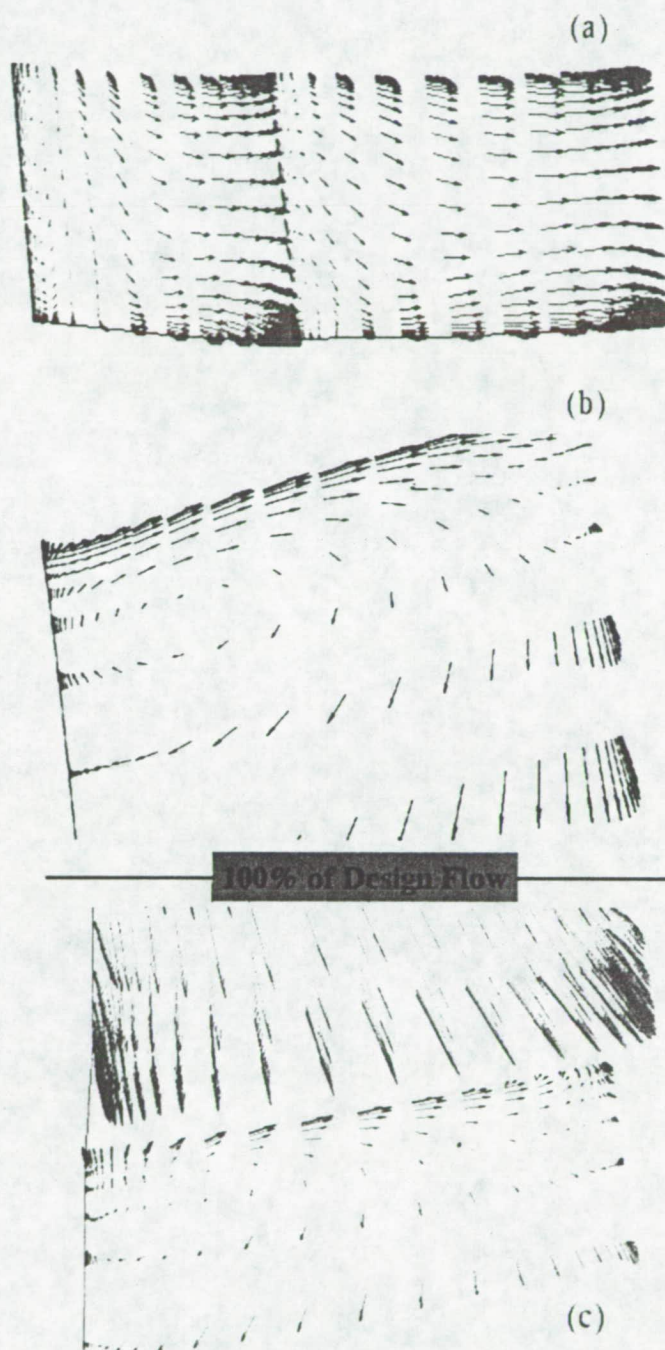


Fig. 19. Relative velocity vectors at impeller exit for design flow case.